



# Large hadron collider constraints on some simple $Z'$ models for $b \rightarrow s\mu^+\mu^-$ anomalies

B. C. Allanach<sup>1,a</sup>, J. M. Butterworth<sup>2,b</sup>, Tyler Corbett<sup>3,c</sup>

<sup>1</sup> Department of Applied Mathematics and Theoretical Physics, University of Cambridge, Wilberforce Road, Cambridge CB3 0WA, UK

<sup>2</sup> Department of Physics and Astronomy, University College London, Gower St, London WC1E 6BT, UK

<sup>3</sup> The Niels Bohr International Academy, University of Copenhagen, Blegdamsvej 17, 2100 Copenhagen, Denmark

Received: 8 November 2021 / Accepted: 6 December 2021  
© The Author(s) 2021

**Abstract** We examine current Large Hadron Collider constraints on some simple  $Z'$  models that significantly improve on Standard Model fits to  $b \rightarrow s\mu^+\mu^-$  transition data. The models that we consider are the ‘third family baryon number minus second family lepton number’ ( $B_3 - L_2$ ) model and the ‘third family hypercharge’ model and variants. The constraints are applied on parameter regions of each model that fit the  $b \rightarrow s\mu^+\mu^-$  transition data and come from high-mass Drell–Yan di-muons and measurements of Standard Model processes. This latter set of observables place particularly strong bounds upon the parameter space of the  $B_3 - L_2$  model when the mass of the  $Z'$  boson is less than 300 GeV.

## 1 Introduction

Certain experimental measurements of particular  $B$  hadron decays are currently in tension with Standard Model (SM) predictions. The ratios of branching ratios  $BR(B \rightarrow K^{(*)}\mu^+\mu^-)/BR(B \rightarrow K^{(*)}e^+e^-)$  [1–3],  $BR(B_s \rightarrow \mu^+\mu^-)$  [4–8], angular distributions in  $B \rightarrow K^*\mu^+\mu^-$  decays [9–14] and the branching ratio  $BR(B \rightarrow \phi\mu^+\mu^-)$  [15, 16] are some examples, which we dub collectively as ‘ $b \rightarrow s\mu^+\mu^-$  anomalies’. Some of these observables have small theoretical uncertainties in their SM predictions, whereas others have more sizeable theoretical uncertainties. No individual measurement is yet in sufficient tension to claim unambiguous  $5\sigma$  evidence of new physics. However, collectively, the tensions point to the same conclusion even when theoretical uncertainties are taken into account: that a beyond the SM (BSM) contribution to a process connecting a left-handed bottom quark  $b_L$ , a left-handed

strange quark  $s_L$ , a muon  $\mu^-$  and an anti-muon  $\mu^+$  is preferred (together with the anti-particle copy of the process).<sup>1</sup> One recent estimate puts the combined global significance at 3.9 standard deviations [18] once the look elsewhere effect and theoretical uncertainties are taken into account. Recent fits to single BSM effective field theory operators broadly agree with each other [19–21]: a correction to the coefficient of the effective field theory operator  $(\bar{b}_L\gamma^\mu s_L)(\bar{\mu}\gamma_\mu P_X\mu)$  in the Lagrangian density can greatly ameliorate the tension between the predictions and the measurements. Here,  $P_X$  is a helicity projection operator. According to the fits, both  $P_X = P_L$  (a coupling to left-handed muons) as well as  $P_X = 1$  (i.e. a vector-like coupling to muons) work approximately as well as each other, but  $P_X = P_R$  is disfavoured. The fits are typically done in the approximation that the energy scale (here given by the bottom meson mass  $m_B$ ) relevant to the measured observables is much smaller than the scale of new physics producing the operator.

A BSM contribution to such effective field theory operators can be generated by the tree-level exchange of a massive electrically-neutral gauge boson (dubbed a  $Z'$ ), as depicted in Fig. 1, if it has family dependent couplings. In particular, to generate the effective field theory operator required, it should have a coupling both to muon/anti-muon fields and to  $\bar{b}_L s_L + \bar{s}_L b_L$ . In the fits of a BSM effective field theory operator to the measurements, terms of order  $m_B^2/M_{Z'}^2$  are implicitly neglected in the effective field theory expansion, where  $M_{Z'}$  is the mass of the  $Z'$  boson.

In order to explain the  $b \rightarrow s\mu^+\mu^-$  anomalies with such a  $Z'$ , the product of the  $Z'$ -coupling to  $\bar{b}_L s_L + \bar{s}_L b_L$  and its coupling to  $\mu^+\mu^-$  divided by  $M_{Z'}^2$  has a range of values

<sup>a</sup> e-mail: B.C.Allanach@damtp.cam.ac.uk

<sup>b</sup> e-mail: j.butterworth@ucl.ac.uk

<sup>c</sup> e-mail: corbett.t.s@gmail.com (corresponding author)

<sup>1</sup> Although their tensions with SM predictions are mild, recent experimental determinations of the ratios of branching ratios  $BR(B^0 \rightarrow K_S^0\mu^+\mu^-)/BR(B^0 \rightarrow K_S^0e^+e^-)$  and  $BR(B^+ \rightarrow K^{(*)+}\mu^+\mu^-)/BR(B^+ \rightarrow K^{(*)+}e^+e^-)$  bolster this conclusion further [17].

**Fig. 1** A tree-level  $Z'$  boson mediated contribution to the  $b \rightarrow s\mu^+\mu^-$  transition

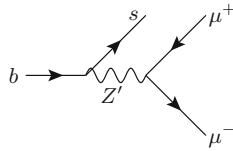
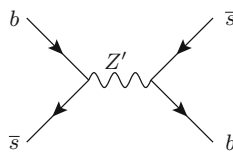


**Fig. 2** Tree-level Feynman diagram of a  $Z'$ -mediated process which contributes to  $B_s - \bar{B}_s$  mixing



that does not include zero. It is then of interest to ask if such a  $Z'$  boson could be produced directly at high energy proton-proton ( $pp$ ) colliders and detected so as to provide a smoking-gun signal of the model. The most obvious decay channel is into  $\mu^+\mu^-$ : the  $\bar{b}_L s_L + \bar{s}_L b_L$  coupling is strongly bounded from above by  $B_s - \bar{B}_s$  mixing constraints, where the data and SM prediction are consistent with each other, but where tree-level  $Z'$  contributions from the diagram in Fig. 2 are predicted. It was shown in Refs. [22,23] that one expects a 100 TeV future circular hadron-hadron collider to be able to cover much of the available parameter space of generic toy  $Z'$  models in the  $\mu^+\mu^-$  channel in parameter regions consistent with the  $b \rightarrow s\mu^+\mu^-$  anomalies. Such searches have been carried out by the Large Hadron Collider (LHC) general purpose experiments ATLAS and CMS, but so far no significant signal has been found. Constraints from a  $139 \text{ fb}^{-1}$  13 TeV  $pp$  ATLAS high-mass Drell–Yan di-lepton search were placed upon the toy models in Ref. [24]. The parameter spaces of toy models which fit the  $b \rightarrow s\mu^+\mu^-$  data were only weakly constrained by the search. However, a more complete model, the Third Family Hypercharge ( $Y_3$ ) Model [25], was found to be more strongly constrained by the search; in particular, it was found that  $M_{Z'} > 1.2 \text{ TeV}$ , calculated in the tree-level limit with an on-shell  $Z'$  (and not including associated production with a jet). Here, the fit to the  $b \rightarrow s\mu^+\mu^-$  data was rather crude: dominant tree-level effects from a SM effective field theory operator were included, and all renormalisation effects were ignored.

In the  $Y_3$  model as well as other typical explicit models, massive  $Z'$  gauge bosons originate from spontaneously broken  $U(1)$  gauge symmetries. Several other models with additional  $U(1)$  gauge symmetries<sup>2</sup> and family dependent charges have been proposed to obtain a  $Z'$  with the correct properties to explain the  $b \rightarrow s\mu^+\mu^-$  anomalies [27–60]. A variant of the  $Y_3$  model, the Deformed Third Family Hypercharge ( $DY_3$ ) was introduced in Ref. [61] where limits from the ATLAS high-mass Drell–Yan di-lepton search were placed upon it. However, the global fits to the  $Y_3$  model and  $DY_3$  model have subsequently changed significantly from the inclusion of precision electroweak observ-

ables, which tend to pull the fit more toward the SM limit [62]. A new variant ( $DY'_3$ ) was introduced in Ref. [62] and a fit of the model to electroweak and  $b \rightarrow s\mu^+\mu^-$  data was performed. The aforementioned ATLAS high-mass Drell–Yan di-lepton search has also constrained the parameter space of the baryon number minus second family lepton number ( $B_3 - L_2$ ) model [45,46]. In the  $B_3 - L_2$  model, in contrast to the third family hypercharge type models, a region of parameter space with  $M_{Z'} < 300 \text{ GeV}$  was found to simultaneously explain the  $b \rightarrow s\mu^+\mu^-$  anomalies and pass all of the other relevant experimental constraints [46]. Such low values of  $M_{Z'}$  are unfeasible in third family hypercharge type models because the fit to electroweak data would become too poor.

Our aim here is to update LHC constraints on the parameter space regions of the  $Y_3$ ,  $DY_3$ ,  $DY'_3$  and  $B_3 - L_2$  models that fit the  $b \rightarrow s\mu^+\mu^-$  anomalies. For the first three models in this list, the good-fit parameter space has changed significantly due to the inclusion of electroweak precision observables in the fit of Ref. [62] (pertinent new data from LHCb were included and the theory predictions were improved to include a proper matching to the SM effective field theory calculation and renormalisation effects, but these had a less dramatic effect). We will check the constraints coming from measurements of SM-predicted processes on the  $DY_3$ ,  $DY'_3$  and  $B_3 - L_2$  models for the first time. Notably, we shall show that the  $M_{Z'} < 300 \text{ GeV}$  region of the  $B_3 - L_2$  model is strongly constrained by such measurements. The calculation of high-mass Drell–Yan di-lepton search constraints upon the  $DY'_3$  model is also new. The calculation of limits in the higher mass régimes of the models is more accurate than previous determinations in the literature because it includes associated production of a jet.<sup>3</sup>

The paper proceeds as follows: the models are defined in Sect. 2 along with a characterisation for each model of the parameter region that fits the  $b \rightarrow s\mu^+\mu^-$  anomalies. In Sect. 3, we then go on to introduce the various measurements used to constrain the models, which are calculated by the CONTUR2.2.0 computer program [63,64]. We present the resulting constraints in Sect. 4 before summarising and discussing them in Sect. 5.

## 2 Models

In this section we shall introduce the four models under study in the present paper. The chiral fermion content of each model is that of the SM augmented by three right-handed neutrinos ( $\text{SM}+3\nu_R$ ); these are added in order to obtain neutrino

<sup>2</sup> However, see Ref. [26] for a case where the  $U(1)$  gauge symmetry comes explicitly embedded within a larger non-abelian symmetry.

<sup>3</sup> Associated production of a jet is calculated in the present paper with transverse momentum cut-off at 20 GeV on the outgoing legs of the two-to-two matrix elements.

masses. Each model extends the SM gauge group by an additional  $U(1)$  gauge group factor and each is anomaly-free. In order to distinguish it from  $U(1)_Y$ , we shall call the additional  $U(1)$  gauge group  $U(1)_X$ .  $U(1)_X$  is broken by the vacuum expectation value ( $\theta$ ) of a SM-singlet complex scalar  $\theta$ , the flavon, which has a non-zero  $U(1)_X$  charge  $X_\theta$ . Then, the  $U(1)_X$  gauge boson  $X^\mu$  acquires a mass via the Brout–Englert–Higgs mechanism,

$$M_X = g_X X_\theta \langle \theta \rangle, \tag{1}$$

where  $g_X$  is the  $U(1)_X$  gauge coupling. The family dependent charges of the other fields are given in Table 1 for the four models under study. We use the following notation for the representation of the chiral fermion fields under  $(SU(3), SU(2), U(1)_Y)$ , where  $i \in \{1, 2, 3\}$  is a family index:  $Q'_{L_i} := (u'_{L_i}, d'_{L_i})^T \sim (\mathbf{3}, \mathbf{2}, 1/6)$ ,  $u'_{R_i} \sim (\mathbf{3}, \mathbf{1}, 2/3)$ ,  $d'_{R_i} \sim (\mathbf{3}, \mathbf{1}, -1/3)$ ,  $e'_{R_i} \sim (\mathbf{1}, \mathbf{1}, -1)$  and  $L'_{L_i} := (v'_{L_i}, e'_{L_i})^T \sim (\mathbf{1}, \mathbf{2}, -1/2)$  and the  $L$  and  $R$  suffix refers to left and right-handed chiral fermions, respectively. The complex scalar Higgs doublet field transforms as  $H \sim (\mathbf{1}, \mathbf{2}, 1/2)$ . In what follows, we denote 3-component column vectors in family space with bold font, for example  $\mathbf{u}'_L := (u'_{L_1}, u'_{L_2}, u'_{L_3})^T$ .

Each of our models then has  $X^\mu$ -fermion couplings in the Lagrangian density as dictated by the charges of the fermions. For each fermion species

$$F \in \{u_L, d_L, \nu_L, e_L, u_R, d_R, \nu_R, e_R\}, \tag{2}$$

we have a Lagrangian density term

$$\mathcal{L} \supset -g_X \left( \overline{\mathbf{F}'} \not{X} \Lambda^{(F)} \mathbf{F}' \right), \tag{3}$$

where we have defined the three-by-three hermitian matrices  $\Lambda^{(F)} := V_F^\dagger \xi_F V_F$  in terms of the 3 by 3 real diagonal matrices  $\xi^{(F)} := \text{diag}(0, X_{F_2}, X_{F_3})$ . The  $V_F$  matrices are 3 by 3 unitary matrices that transform  $F$  from the (primed) weak eigenbasis to the (unprimed) mass eigenbasis, i.e.  $\mathbf{F}' := V_F \mathbf{F}$ . The CKM matrix  $V$  and the PMNS matrix  $U$  are then predicted to be

$$V = V_{u_L}^\dagger V_{d_L}, \quad U = V_{\nu_L}^\dagger V_{e_L}, \tag{4}$$

respectively.

In order to specify the models further for phenomenological investigation, one must make some assumptions about the  $V_F$  matrices. They are taken to be consistent with (4) once empirical inputs are taken for the central values of the entries of  $U$  and  $V$ . For simplicity, we take  $V_{u_R} = V_{d_R} = V_{e_R} = V_{e_L} = I_3$ , the 3 by 3 identity matrix.  $V_{\nu_L} = U$  may be fixed by using empirical inputs for  $U$  (however, neutrinos shall play no further role in our study). We shall require  $V_{d_L} \neq I_3$ ,

since we require a coupling between  $d_{L_2}$  and  $d_{L_3}$  and the  $X^\mu$  boson in order to explain the  $b \rightarrow s\mu^+\mu^-$  anomalies. A ‘standard parameterisation’ [65] of a 3 by 3 unitary matrix<sup>4</sup> was chosen for  $V_{d_L}$ :

$$\begin{pmatrix} c_{12}c_{13} & s_{12}c_{13} & s_{13}e^{-i\delta} \\ -s_{12}c_{23} - c_{12}s_{23}s_{13}e^{i\delta} & c_{12}c_{23} - s_{12}s_{23}s_{13}e^{i\delta} & s_{23}c_{13} \\ s_{12}s_{23} - c_{12}c_{23}s_{13}e^{i\delta} & -c_{12}s_{23} - s_{12}c_{23}s_{13}e^{i\delta} & c_{23}c_{13} \end{pmatrix},$$

where  $s_{ij} := \sin \theta_{ij}$  and  $c_{ij} := \cos \theta_{ij}$ , for angles  $\theta_{ij}$ ,  $\delta \in \mathbb{R}$ .  $\theta_{23}$  was allowed to vary, since it is this coupling that controls the  $X^\mu$  coupling to  $\overline{b_L}s_L + \overline{s_L}b_L$ . The assumptions on the angles and phase in  $V_{d_L}$  in the fits we use are different for the third family hypercharge type models [62] and the  $B_3 - L_2$  model [54], so we consider each in turn.

### 2.1 Third family hypercharge models

In this subsection, we shall characterise recent global fits of the three third family hypercharge type models under investigation ( $Y_3, DY_3$  and  $DY'_3$ ) to  $b \rightarrow s\mu^+\mu^-$  data [62]. Aside from the effects of varying  $\theta_{23}$ , we set  $V_{d_L}$  equal to the CKM matrix. In more detail, the other angles and phases in  $V_{d_L}$  are set equal to the central values of the parameters of the CKM matrix inferred by experimental measurements, i.e.  $s_{12} = 0.22650$ ,  $s_{13} = 0.00361$  and  $\delta = 1.196$  [65].

$X_H \neq 0$  in third family hypercharge type models (as Table 1 attests) implying that they predict ‘ $Z^0$ - $Z'$  mixing’ (i.e. mixing between the  $X^\mu$  boson, the hypercharge gauge boson and the electrically neutral  $SU(2)_L$  boson) and thus they affect the prediction of precision electroweak observables. Ref. [62] went on to fit the third family hypercharge type models to 219 electroweak and  $b \rightarrow s\mu^+\mu^-$  data. The effective field theory calculation of observables in the electroweak sector implicitly misses relative corrections of  $\mathcal{O}(M_{Z_0}^2/M_X^2)$  and so is only valid if  $M_X \gg M_{Z_0}$ , the mass of the  $Z^0$  gauge boson. After electroweak symmetry breaking, the mass of the gauge boson is corrected to follow

$$M_{Z'}^2 = M_X^2 [1 + \mathcal{O}(M_{Z_0}^2/M_X^2)]. \tag{5}$$

All three models ( $Y_3, DY_3, DY'_3$ ) provided a much better fit than that of the SM: improving  $\Delta\chi^2$  by 33–43 units depending upon the model, for two fitted parameters ( $\theta_{23}$  and  $g_X/M_X$ ). The 95% confidence level (CL) region of each model is shown in Fig. 3 as a shaded region, as according to the legend. We wish to reduce the three independent parameters ( $g_X, M_X$  and  $\theta_{23}$ ) down to two in order to display search

<sup>4</sup> The standard parameterisation parameterises a family of unitary 3 by 3 matrices that depends only upon one complex phase and three mixing angles; a more general parameterisation would also depend upon five additional complex phases.

**Table 1**  $U(1)_X$  charges  $X_{\phi'}$  of weak eigenbasis fields  $\phi'$  in each model. SM+ $3\nu_R$  fields that are not listed for a model have a zero charge. In addition, each model possesses a complex scalar flavon field  $\theta$  of  $U(1)_X$  charge  $X_\theta$

$Y_3$	$Q'_{L_3}$	$e'_{R_3}$	$u'_{R_3}$	$d'_{R_3}$	$L'_{L_2}$	$H$	
	1/6	-1	2/3	-1/3	-1/2	1/2	
$DY_3$	$Q'_{L_3}$	$e'_{R_3}$	$u'_{R_3}$	$d'_{R_3}$	$L'_{L_2}$	$e'_{R_2}$	$L'_{L_3}$
	1/6	-5/3	2/3	-1/2	5/6	2/3	-4/3
	$e'_{R_3}$	$H$					
	-5/3	1/2					
$DY'_3$	$Q'_{L_3}$	$e'_{R_3}$	$u'_{R_3}$	$d'_{R_3}$	$L'_{L_2}$	$e'_{R_2}$	$L'_{L_3}$
	1/6	-5/3	2/3	-1/2	-4/3	2/3	5/6
	$e'_3$	$H$					
	-5/3	1/2					
$B_3 - L_2$	$Q'_{L_3}$	$e'_{R_2}$	$u'_{R_3}$	$d'_{R_3}$	$L'_{L_2}$	$\nu'_{R_2}$	$H$
	1	-3	1	1	-3	-3	0

constraints in terms of two-dimensional plots. To this end, we characterise each fit in Fig. 3 by a dashed curve. The equation of each curve is parameterised by

$$\theta_{23} = \frac{1}{2} \sin^{-1} \left( \frac{a}{x^2 + bx} \right), \tag{6}$$

where

$$x := g_X(1 \text{ TeV}/M_X) \tag{7}$$

and  $a$  and  $b$  were ‘fit by eye’ for each model. The values taken, along with the domain of good fit, are displayed in Table 2 for each model. It will suit us below to scan in  $x$  and  $M_X \approx M_{Z'}$ , constraining  $\theta_{23}$  to satisfy (6) in order to stay within the region of good fit for the domain of  $x$  given in Table 2. We shall refer to this region, where flavour data (and electroweak data for the third-family hypercharge type models) are within the 95% CL, as the ‘favoured region’ of each model.

### 2.2 $B_3 - L_2$ model

In the  $B_3 - L_2$  model [45,46], since  $X_H = 0$ , there is no  $Z^0 - Z'$  mixing at tree-level and so  $M_{Z'} = M_X$ . Electroweak precision observables then follow the SM predictions, to a good approximation. We may thus entertain lower values of  $M_{Z'}$ , since neither the theoretical consistency constraint nor the need to avoid large corrections to SM predictions of electroweak observables (both of which imply  $M_X \gg M_{Z^0}$  in third family hypercharge type models) apply to the  $B_3 - L_2$  model. Ref. [46] showed that, as well as possessing viable  $M_{Z'} > 1 \text{ TeV}$  parameter space, the model has a region of parameter space within the domain  $20 \text{ GeV} < M_X < 300 \text{ GeV}$  which simultaneously evades other constraints whilst providing much improved fits to  $b \rightarrow s\mu^+\mu^-$  data.

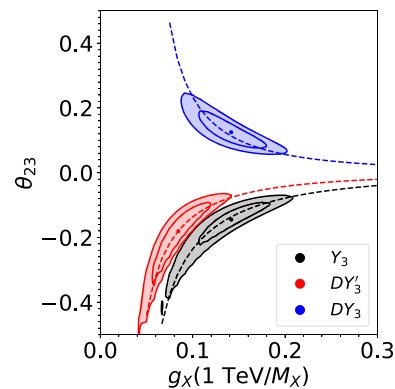


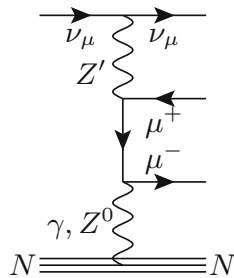
**Fig. 3** Global fits of third family hypercharge models from Ref. [62] for  $M_X = 3 \text{ TeV}$ . The shaded regions are the 95% CL fit regions for the model, as according to the legend. The inner contours within each shaded region enclose the 68% CL region. The parameter point of best-fit is labelled by a dot in each case. To a good approximation, the fits are independent of  $M_X$ , provided that it is much larger than  $M_{Z^0}$  and provided that  $g_X$  is scaled proportional to  $M_X$ , as implied by the abscissa [62]. We show our characterisation of the good-fit region by the dashed line in each case, detailed in (6) and Table 2

**Table 2** Parameterisation values and domain of  $x$  for the 95% CL region for each model, as described by (6). In the  $B_3 - L_2$  model, there is no currently calculated upper bound for  $x$

Model	$a$	$b$	$x$
$Y_3$	-0.01	0.12	0.08–0.2
$DY_3$	0.0045	0	0.1–0.2
$DY'_3$	-0.0045	0.067	0.04–0.13
$B_3 - L_2$	-0.0005	0	0.05–0.62

The  $B_3 - L_2$  model was matched to fits of  $b \rightarrow s\mu^+\mu^-$  data in Ref. [54]. The assumptions on  $V_{dL}$  were equivalent to taking  $s_{12} = s_{13} = \delta = 0$  in (6) and it was found, after matching to the  $b \rightarrow s\mu^+\mu^-$  fit, that  $\theta_{23}$  satisfies (6) with

**Fig. 4** Tree-level Feynman diagram of a  $Z'$  contribution to the neutrino trident process.  $N$  represents a nucleon



the values shown in Table 2. The upper bound on the domain of  $x$  comes from measurements of the trident process, which roughly agree with SM predictions and so cannot receive large corrections from the  $Z'$ -mediated process shown in Fig. 4. The lower bound on the domain of  $x$  comes from measurements of  $B_s - \bar{B}_s$  mixing, which bounds the contribution coming from the process in Fig. 2. We note in passing that the fit we match to in the  $B_3 - L_2$  model taken is less sophisticated than the global fits used for the third family hypercharge type models; the fit to the  $B_3 - L_2$  model was at the tree-level and did not include renormalisation group effects. In contrast to the third family hypercharge type models, the predictions of the  $B_3 - L_2$  model for electroweak observables are identical to those of the SM and so they were not included in the fit.

### 3 LHC constraints from CONTUR

The  $Z'$ -fermion interactions of the four models that we use have been encoded into UFO format [66]<sup>5</sup> by using FEYNRULES [67]. Currently, the flavon is neglected in the files, however  $Z^0 - Z'$  mixing effects [25] have been included to leading order in  $(M_{Z^0}/M_{Z'})^2$  for the third-family hypercharge type models.

The UFO files are then passed to the HERWIG7.2.2 [68,69] event generator, which calculates the total width and branching fractions of the  $Z'$ , and generates full final-state simulated  $pp$  collision events.<sup>6</sup> These events are passed through the RIVET3.1.5 [70] library of analyses. This constitutes a ‘signal injection’ of the putative BSM contribution to several hundred differential cross-sections measured at the LHC and stored in HEPDATA [71]. CONTUR then evaluates whether this BSM contribution would have been visible given the experimental uncertainties, and if it should have been ‘seen already’, derives an exclusion probability. The approach is described in more detail in [64].

<sup>5</sup> The UFO and FEYNRULES files are included in the ancillary information attached to the arXiv version of this paper, and will be bundled with future releases of CONTUR.

<sup>6</sup> The main resonant  $Z'$  production process cross-section was checked against MADGRAPH 2.6.5 and found to be consistent.

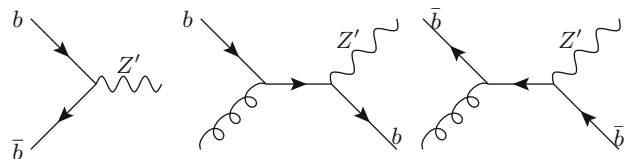


**Fig. 5** Dominant Feynman diagrams of tree-level inclusive  $Z'$  production at the LHC. The two right-most diagrams are examples of associated production (of a  $Z'$  with a  $b$ -jet or an anti- $b$ -jet)

### 4 Results

We find that high-mass Drell–Yan LHC searches into a di-muon final state provide the most constraining bound at large values of  $M_{Z'}$ , irrespective of the model. The dominant partonic  $Z'$  production processes are shown in Fig. 5, where it is emphasised that one requires a  $b\bar{b}$  partonic initial state from the LHC proton pairs  $pp$ . The calculated  $Z'$  production cross-section is thus dependent upon which parton distribution function (PDF) set is used, since the  $b(\bar{b})$  content of the proton differs from PDF-set to PDF-set at relatively high values of the ratio of partonic centre of mass energy to  $pp$  centre of mass energy<sup>7</sup> For the results discussed below, the default HERWIG 7.2.2 choice of CT14 [72] was used.

The exclusion limit for the  $Y_3$  model is shown in Fig. 6. The sensitivity is dominated by the di-muon channel in the high-mass ATLAS Drell–Yan di-lepton search, with the CMS measurement [73] (which uses only  $3.2 \text{ fb}^{-1}$  of integrated luminosity) also contributing. The data barely impinge on the allowed parameter space, with only a small region at low mass and large coupling disfavoured. Here, we see that the favoured region  $g_X < 0.2$  is not constrained at the 95% CL in the parameter space considered.

For the  $DY_3$  model, Fig. 7 shows that the sensitivity is somewhat greater, extending to  $M_{Z'} \approx 1.2 \text{ TeV}$  for the highest values of  $g_X \times 1 \text{ TeV}/M_{Z'}$  considered, with the same two datasets contributing. At low  $M_{Z'}$ , the favoured region  $0.1 \leq g_X \times 1 \text{ TeV}/M_{Z'} \leq 0.2$  is constrained by the ATLAS high-mass Drell–Yan  $ll$  search at the 95% CL.

The exclusion is stronger still for the  $DY'_3$  model, shown in Fig. 8. At high coupling, masses up to  $M_{Z'} \approx 1.3 \text{ TeV}$  are excluded, although in the region favoured by the fits, only the low  $M_{Z'}$  region is impacted.

The comparative strength of the bounds in the three third family hypercharge models can be understood in terms of the size of the absolute additional  $U(1)$  charges of the left-handed and right-handed muons. For a given point in parameter space, the larger the absolute value of the charge, the larger is  $BR(Z' \rightarrow \mu^+ \mu^-)$  and so the bound from high mass Drell–

<sup>7</sup> We observed some 20% differences in the calculated production cross-section when changing the PDF set used.

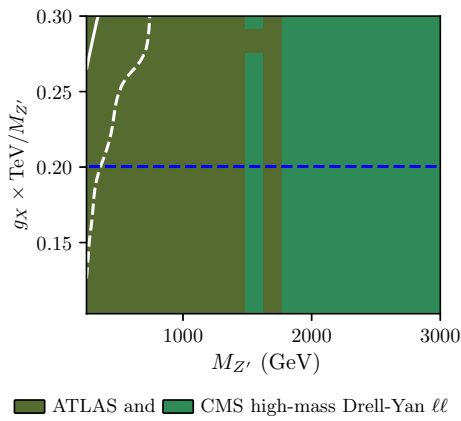


**Fig. 6** Exclusion in the parameter plane for the  $Y_3$  model. The colours indicate the bound giving the dominant sensitivity as in the key below. The region above the white solid line is excluded at the 95% CL and the region above the white dashed line is excluded at the 68% CL. The region favoured by the fits is below the blue dashed line

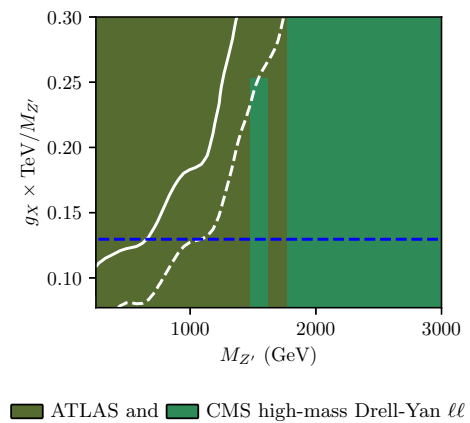


**Fig. 8** Exclusion in the parameter plane for  $DY_3'$  model. The colours indicate the bound giving the dominant sensitivity as in the key below. The region above the white solid line is excluded at the 95% CL and the region above the white dashed line is excluded at the 68% CL. The region favoured by the fits is below the blue dashed line

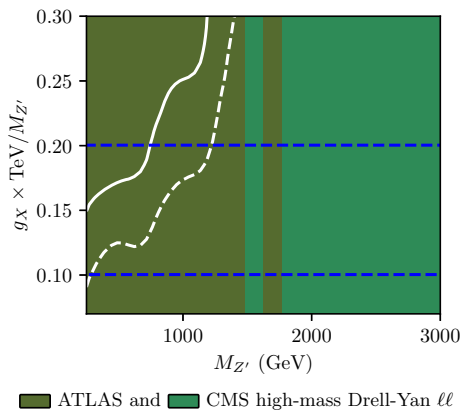


**Fig. 7** Exclusion in the parameter plane for  $DY_3$  model. The colours indicate the bound giving the dominant sensitivity as in the key below. The region above the white solid line is excluded at the 95% CL and the region above the white dashed line is excluded at the 68% CL. The region favoured by the fits is between the blue dashed lines

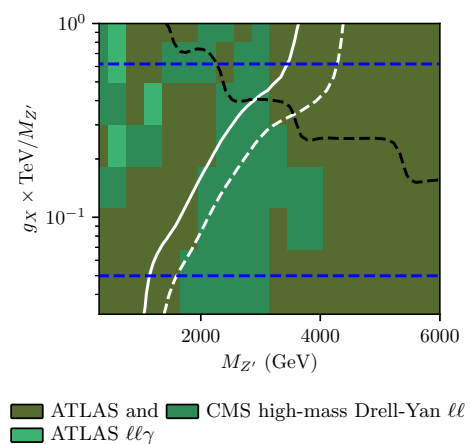


**Fig. 9** Exclusion in the high mass region of the  $B_3 - L_2$  model. The colours indicate the bound giving the dominant sensitivity as in the key below. The region above the white solid line is excluded at the 95% CL and the region above the white dashed line is excluded at the 68% CL. In the region above the black dashed line, the width of the  $Z'$  is more than  $M_{Z'}/3$ , and so the perturbative cross-section calculation becomes unreliable. The region favoured by the fits is between the blue dashed lines

Yan di-lepton searches is concomitantly stronger.<sup>8</sup> As a careful reading of Table 1 allows, whilst the quark charges are identical for the three models in question, the muon charges are largest for the  $DY_3'$  model, next largest for the  $DY_3$  model and smallest for the  $Y_3$  model, allowing a rough understanding of the comparative strength of the high mass Drell–Yan bounds within each.

For the  $B_3 - L_2$  model, the range  $200 < M_{Z'} < 1000$  GeV is excluded for all allowed couplings, as shown in Fig. 9. In this case di-lepton-plus-photon final states [74–76] also contribute. At high couplings the limit extends

<sup>8</sup> Strictly speaking,  $BR(Z' \rightarrow \mu^+\mu^-)$  also depends upon the third family lepton charges (which differ between the three models). Taking this into account for the models in question, it is still true that  $BR(Z' \rightarrow \mu^+\mu^-)$  is ordered by the comparative absolute value of the muonic charges.

up to around 3.7 TeV. However, as previously mentioned, in this model an open parameter window at low masses  $M_{Z'} < 300$  GeV also exists.

In Fig. 10, we examine this low-mass region. The picture in terms of contributing analyses is more complex. Di-lepton measurements at the  $Z^0$  pole, particularly those in Refs. [77, 78], exclude much of the region for  $g_X \times 1 \text{ TeV}/M_{Z'} > 1$ . Measurements targeted at  $W$  bosons decaying leptonically [79–81] play the dominant role around  $M_{Z'} = 300$  GeV for high couplings. Photon-plus-di-lepton measurements again contribute, especially at higher masses and lower couplings. Lower mass di-lepton measurements [82] contribute for  $M_{Z'} < M_{Z^0}$ . In the region where the sensitivity runs out, the

**Table 3** Example leading order matrix element cross-sections calculated by HERWIG for some parameter points for the four models considered. The cross-sections quoted are  $pp$  cross-sections at 13 TeV centre-of-mass energy, in fb.  $\sigma_{Z'+q,g}$  is the cross-section for associated

$Z'$ -quark production plus the cross-section for associated  $Z'$ -gluon production, with a minimum transverse momentum of 20 GeV for the quark or gluon

Model	$M_{Z'}$ (GeV)	$x$	$\sigma_{Z' \rightarrow \mu^+\mu^-}$ exclusive	$\sigma_{Z'+q,g}$	$\sigma_{Z'+\gamma}$
$Y_3$	540	0.2	0.7	10	0.02
$DY_3$	540	0.2	3.3	31	0.06
$DY'_3$	540	0.2	5.7	26	0.07
$B_3 - L_2$	60	0.074	600	750	0.4

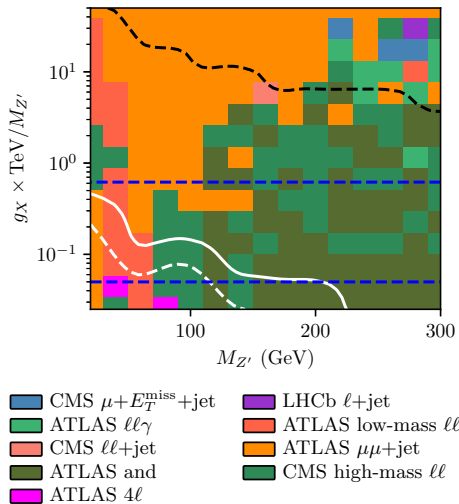


**Fig. 10** Exclusion in the low mass region of the  $B_3 - L_2$  model. The colours indicate the bound giving the dominant sensitivity as in the key below. The region above the white solid line is excluded at the 95% CL and the region above the white dashed line is excluded at the 68% CL. In the region above the black dashed line, the width of the  $Z'$  is more than  $M_{Z'}/3$ , and so the perturbative cross-section calculation becomes unreliable. The region favoured by the fits is between the blue dashed lines

inclusive four-lepton measurement [83] also contributes, due to a clean (but very low cross-section) ( $Z'$   $Z^0$ )-production contribution. With more integrated luminosity this observable would become more sensitive.

The fact that the cross-section for this model is large enough to significantly distort the expected distributions, even in the presence of a large SM cross-section, means that the model is disfavoured over the majority of the previously open parameter window, leaving only a small region at low mass and low values of  $g_X \times 1 \text{ TeV}/M_{Z'}$  still allowed. We note that towards the left-hand side of the plot, the accuracy of the previous fit of the model to flavour data is called into question since unaccounted-for relative corrections  $\mathcal{O}(m_B^2/M_{Z'}^2)$  become sizeable.

For an example point in parameter space for each model, we display some relevant cross-sections in Table 3.

### 5 Summary and discussion

We have calculated LHC bounds upon four models that have been fitted to  $b \rightarrow s\mu^+\mu^-$  anomalies. Each of the models includes an electrically neutral, massive  $Z'$  gauge boson which has family dependent couplings to SM fermions, the most important for our discussion being the couplings to  $\mu^+\mu^-$  and to  $\bar{b}s + b\bar{s}$ .<sup>9</sup>

Three third family hypercharge type models (the  $Y_3$ ,  $DY_3$  and  $DY'_3$  models) were recently fit [62] to  $b \rightarrow s\mu^+\mu^-$  data, which is in tension with SM predictions. The fits included electroweak data, since the third family hypercharge models alter the SM predictions of the electroweak observables. In the present paper, we have calculated LHC constraints upon the parameter space of these three models that fit the  $b \rightarrow s\mu^+\mu^-$  data. The LHC constraints upon the three third family hypercharge models are much weaker than those calculated previously in Refs. [24, 61]. This is due to the fact both the electroweak data and recent  $b \rightarrow s\mu^+\mu^-$  data pushed the fit towards the SM limit, preferring smaller values of  $g_X \times 1 \text{ TeV}/M_{Z'}$  as compared to previous preferred values. Our calculation is at a higher level of precision compared to previous estimates, since it includes the effects of associated production and renormalisation of the SM effective field theory in the fit. Neither the  $DY_3$  model nor the  $DY'_3$  model had been checked previously against measurements of SM-predicted processes. However, for the parameter regions of interest where  $M_{Z'} > 300 \text{ GeV}$ , these are not as constraining as the high-mass Drell–Yan di-lepton searches, as Figs. 6, 7 and 8 show. In general even the high-mass Drell–Yan limits upon the third family hypercharge models are not very constraining; one cannot quote a lower bound on  $M_{Z'}$  independent of the coupling for any of the three models.

<sup>9</sup> In principle, a  $Z'$  coupling to  $\mu^+\mu^-$  can change the prediction of the anomalous magnetic moment of the muon  $a_\mu$ , which has been measured to be in tension with its SM prediction [84]. However, in order to satisfy other experimental constraints, simple  $Z'$  models such as those deployed in the present paper are forced into a parameter space where the beyond-the-SM contribution to  $a_\mu$  from the  $Z'$  is too small to explain the discrepancy and so further model building involving additional fields and/or additional  $Z'$  couplings [85] would be required to explain the measured value of  $a_\mu$ .

In contrast, the  $B_3 - L_2$  model is more tightly constrained by the high-mass Drell–Yan di-lepton searches at the LHC, as Fig. 9 shows:  $M_{Z'} > 1$  TeV in the favoured region. The measurements of SM-predicted quantities (calculated here for the first time) have a large impact on the low  $M_{Z'}$  window of the  $B_3 - L_2$  model, as shown in Fig. 10. Differential cross-sections in an ATLAS  $\mu\mu$ +jet analysis play a particularly important role at low  $M_{Z'}$ . The constraints in the low  $M_{Z'}$  window are significantly stronger than those calculated previously in Refs. [46, 54].

Generally, measuring  $\tau$  leptons is more difficult than measuring muons in LHC experiments. However, at higher transverse momenta, the hadronic  $\tau$  energy resolution is expected to improve [86], since it is dominated by calorimetry, whereas the muon resolution degrades, due to the lower curvature in the trackers [87, 88]. Higher values of  $M_{Z'}$  lead to final state particles at higher transverse momenta on average, so  $\tau$  leptons may become relatively more important. We note that while no relevant measurements of  $\tau$  final states are currently available in RIVET, for the  $Y_3$  model, the branching fraction  $Z' \rightarrow \tau^+\tau^-$  is around<sup>10</sup> 0.3, compared to  $Z' \rightarrow \mu^+\mu^- \approx 0.075$ . For  $DY_3$  the corresponding branching fractions are 0.4 and 0.1, and for  $DY_3'$  0.35 and 0.22, suggesting that  $\tau$  measurements could make an important contribution in future, despite the additional experimental challenges involved.

For each of the four models that we analyse, an appreciable portion of parameter space remains where future LHC analyses may search for (and hopefully find) a signal.

**Acknowledgements** This work has been partially supported by STFC consolidated Grants ST/N000285/1, ST/P000681/1 and ST/T000694/1. This work has received funding from the European Union’s Horizon 2020 research and innovation programme as part of the Marie Skłodowska-Curie Innovative Training Network MCnetITN3 (Grant Agreement No. 722104). BCA thanks other members of the Cambridge Pheno Working Group for helpful interactions. We especially thank H Banks for helpful high-mass Drell–Yan di-lepton cross-section and limit comparisons in the  $Y_3$  model.

**Data Availability Statement** This manuscript has associated data in a data repository. [Authors’ comment: Supplementary data and a script for plotting Figure 3 is provided. UFO files for the models  $Y_3$ ,  $DY_3$ , and  $DY_3'$  are also provided in the data repository.]

**Open Access** This article is licensed under a Creative Commons Attribution 4.0 International License, which permits use, sharing, adaptation, distribution and reproduction in any medium or format, as long as you give appropriate credit to the original author(s) and the source, provide a link to the Creative Commons licence, and indicate if changes were made. The images or other third party material in this article are included in the article’s Creative Commons licence, unless indicated otherwise in a credit line to the material. If material is not

<sup>10</sup> We quote representative values of the branching fractions in the régime where  $M_{Z'}$  is much greater than twice the top quark mass. The predicted branching fractions we quote here all increase for lower values of  $M_{Z'}$ .

included in the article’s Creative Commons licence and your intended use is not permitted by statutory regulation or exceeds the permitted use, you will need to obtain permission directly from the copyright holder. To view a copy of this licence, visit <http://creativecommons.org/licenses/by/4.0/>.  
Funded by SCOAP<sup>3</sup>.

## References

1. LHCb Collaboration, R. Aaij et al., Test of lepton universality with  $B^0 \rightarrow K^{*0}\ell^+\ell^-$  decays. JHEP **08**, 055 (2017). [arXiv:1705.05802](https://arxiv.org/abs/1705.05802)
2. LHCb Collaboration, R. Aaij et al., Search for lepton-universality violation in  $B^+ \rightarrow K^+\ell^+\ell^-$  decays. Phys. Rev. Lett. **122**(19), 191801 (2019). [arXiv:1903.09252](https://arxiv.org/abs/1903.09252)
3. LHCb Collaboration, R. Aaij et al., Test of lepton universality in beauty-quark decays. [arXiv:2103.11769](https://arxiv.org/abs/2103.11769)
4. ATLAS Collaboration, M. Aaboud et al., Study of the rare decays of  $B_s^0$  and  $B^0$  mesons into muon pairs using data collected during 2015 and 2016 with the ATLAS detector. JHEP **04**, 098 (2019). [arXiv:1812.03017](https://arxiv.org/abs/1812.03017)
5. CMS Collaboration, S. Chatrchyan et al., Measurement of the  $B_s^0 \rightarrow \mu^+\mu^-$  Branching Fraction and Search for  $B^0 \rightarrow \mu^+\mu^-$  with the CMS experiment. Phys. Rev. Lett. **111**, 101804 (2013). [arXiv:1307.5025](https://arxiv.org/abs/1307.5025)
6. CMS, LHCb Collaboration, V. Khachatryan et al., Observation of the rare  $B_s^0 \rightarrow \mu^+\mu^-$  decay from the combined analysis of CMS and LHCb data. Nature **522**, 68–72 (2015). [arXiv:1411.4413](https://arxiv.org/abs/1411.4413)
7. LHCb Collaboration, R. Aaij et al., Measurement of the  $B_s^0 \rightarrow \mu^+\mu^-$  branching fraction and effective lifetime and search for  $B^0 \rightarrow \mu^+\mu^-$  decays. Phys. Rev. Lett. **118**(19), 191801 (2017). [arXiv:1703.05747](https://arxiv.org/abs/1703.05747)
8. LHCb Collaboration, R. Aaij et al., Measurement of the  $B_s^0 \rightarrow \mu^+\mu^-$  decay properties and search for the  $B^0 \rightarrow \mu^+\mu^-$  and  $B_s^0 \rightarrow \mu^+\mu^-\gamma$  decays. [arXiv:2108.09283](https://arxiv.org/abs/2108.09283)
9. LHCb Collaboration, R. Aaij et al., Measurement of form-factor-independent observables in the decay  $B^0 \rightarrow K^{*0}\mu^+\mu^-$ . Phys. Rev. Lett. **111**, 191801 (2013). [arXiv:1308.1707](https://arxiv.org/abs/1308.1707)
10. LHCb Collaboration, R. Aaij et al., Angular analysis of the  $B^0 \rightarrow K^{*0}\mu^+\mu^-$  decay using  $3\text{ fb}^{-1}$  of integrated luminosity. JHEP **02**, 104 (2016). [arXiv:1512.04442](https://arxiv.org/abs/1512.04442)
11. ATLAS Collaboration, M. Aaboud et al., Angular analysis of  $B_d^0 \rightarrow K^{*}\mu^+\mu^-$  decays in  $pp$  collisions at  $\sqrt{s} = 8$  TeV with the ATLAS detector. JHEP **10**, 047 (2018). [arXiv:1805.04000](https://arxiv.org/abs/1805.04000)
12. CMS Collaboration, A. M. Sirunyan et al., Measurement of angular parameters from the decay  $B^0 \rightarrow K^{*0}\mu^+\mu^-$  in proton-proton collisions at  $\sqrt{s} = 8$  TeV. Phys. Lett. B **781**, 517–541 (2018). [arXiv:1710.02846](https://arxiv.org/abs/1710.02846)
13. CMS Collaboration, V. Khachatryan et al., Angular analysis of the decay  $B^0 \rightarrow K^{*0}\mu^+\mu^-$  from pp collisions at  $\sqrt{s} = 8$  TeV. Phys. Lett. B **753**, 424–448 (2016). [arXiv:1507.08126](https://arxiv.org/abs/1507.08126)
14. C. Bobeth, M. Chrzaszcz, D. van Dyk, J. Virto, Long-distance effects in  $B \rightarrow K^*\ell\ell$  from analyticity. Eur. Phys. J. C **78**(6), 451 (2018). [arXiv:1707.07305](https://arxiv.org/abs/1707.07305)
15. LHCb Collaboration, R. Aaij et al., Angular analysis and differential branching fraction of the decay  $B_s^0 \rightarrow \phi\mu^+\mu^-$ . JHEP **09**, 179 (2015). [arXiv:1506.08777](https://arxiv.org/abs/1506.08777)
16. CDF collaboration, Precise measurements of exclusive  $b \rightarrow s\mu + \mu^-$  decay amplitudes using the full CDF Data set. CDF-NOTE-10894 (2012)
17. LHCb Collaboration, R. Aaij et al., Tests of lepton universality using  $B^0 \rightarrow K_S^0\ell^+\ell^-$  and  $B^+ \rightarrow K^{*+}\ell^+\ell^-$  decays. [arXiv:2110.09501](https://arxiv.org/abs/2110.09501)
18. D. Lancierini, G. Isidori, P. Owen, N. Serra, On the significance of new physics in  $b \rightarrow s\ell^+\ell^-$  decays. [arXiv:2104.05631](https://arxiv.org/abs/2104.05631)

19. T. Hurth, F. Mahmoudi, D. M. Santos, S. Neshatpour, More indications for lepton nonuniversality in  $b \rightarrow s\ell^+\ell^-$ . [arXiv:2104.10058](#)
20. W. Altmannshofer, P. Stangl, New physics in rare B decays after moriond (2021). [arXiv:2103.13370](#)
21. M. Algueró, B. Capdevila, S. Descotes-Genon, J. Matias, M. Novoa-Brunet,  $b \rightarrow s\ell\ell$  global fits after Moriond 2021 results, in *55th Rencontres de Moriond on QCD and high energy interactions*, vol. 4 (2021). [arXiv:2104.08921](#)
22. B.C. Allanach, B. Gripaios, T. You, The case for future hadron colliders from  $B \rightarrow K^{(*)}\mu^+\mu^-$  decays. *JHEP* **03**, 021 (2018). [arXiv:1710.06363](#)
23. B.C. Allanach, T. Corbett, M.J. Dolan, T. You, Hadron collider sensitivity to fat flavourful Z's for  $R_{K^{(*)}}$ . *JHEP* **03**, 137 (2019). [arXiv:1810.02166](#)
24. B.C. Allanach, J.M. Butterworth, T. Corbett, Collider constraints on Z' models for neutral current B-anomalies. *JHEP* **08**, 106 (2019). [arXiv:1904.10954](#)
25. B.C. Allanach, J. Davighi, Third family hypercharge model for  $R_{K^{(*)}}$  and aspects of the fermion mass problem. *JHEP* **12**, 075 (2018). [arXiv:1809.01158](#)
26. Y. Chung, A flavorful composite Higgs model: connecting the B anomalies with the hierarchy problem. [arXiv:2108.08511](#)
27. W. Altmannshofer, S. Gori, M. Pospelov, I. Yavin, Quark flavor transitions in  $L_\mu - L_\tau$  models. *Phys. Rev. D* **89**, 095033 (2014). [arXiv:1403.1269](#)
28. A. Crivellin, G. D'Ambrosio, J. Heeck, Explaining  $h \rightarrow \mu^\pm\tau^\mp$ ,  $B \rightarrow K^*\mu^+\mu^-$  and  $B \rightarrow K\mu^+\mu^-/B \rightarrow Ke^+e^-$  in a two-Higgs-doublet model with gauged  $L_\mu - L_\tau$ . *Phys. Rev. Lett.* **114**, 151801 (2015). [arXiv:1501.00993](#)
29. A. Crivellin, G. D'Ambrosio and J. Heeck, Addressing the LHC flavor anomalies with horizontal gauge symmetries. *Phys. Rev. D* **91**(7), 075006 (2015). [arXiv:1503.03477](#)
30. A. Crivellin, L. Hofer, J. Matias, U. Nierste, S. Pokorski, J. Rosiek, Lepton-flavour violating B decays in generic Z' models. *Phys. Rev. D* **92**(5), 054013 (2015). [arXiv:1504.07928](#)
31. W. Altmannshofer, I. Yavin, Predictions for lepton flavor universality violation in rare B decays in models with gauged  $L_\mu - L_\tau$ . *Phys. Rev. D* **92**(7), 075022 (2015). [arXiv:1508.07009](#)
32. D. Aristizabal Sierra, F. Staub, A. Vicente, Shedding light on the  $b \rightarrow s$  anomalies with a dark sector. *Phys. Rev. D* **92**(1), 015001 (2015). [arXiv:1503.06077](#)
33. A. Celis, J. Fuentes-Martin, M. Jung, H. Serodio, Family nonuniversal Z' models with protected flavor-changing interactions. *Phys. Rev. D* **92**(1), 015007 (2015). [arXiv:1505.03079](#)
34. A. Greljo, G. Isidori, D. Marzocca, On the breaking of lepton flavor universality in B decays. *JHEP* **07**, 142 (2015). [arXiv:1506.01705](#)
35. A. Falkowski, M. Nardecchia, R. Ziegler, Lepton flavor non-universality in B-meson decays from a U(2) Flavor Model. *JHEP* **11**, 173 (2015). [arXiv:1509.01249](#)
36. C.-W. Chiang, X.-G. He, G. Valencia, Z' model for  $b \rightarrow sll$  flavor anomalies. *Phys. Rev. D* **93**(7), 074003 (2016). [arXiv:1601.07328](#)
37. S.M. Boucenna, A. Celis, J. Fuentes-Martin, A. Vicente, J. Virto, Non-abelian gauge extensions for B-decay anomalies. *Phys. Lett. B* **760**, 214–219 (2016). [arXiv:1604.03088](#)
38. S.M. Boucenna, A. Celis, J. Fuentes-Martin, A. Vicente, J. Virto, Phenomenology of an  $SU(2) \times SU(2) \times U(1)$  model with lepton-flavour non-universality. *JHEP* **12**, 059 (2016). [arXiv:1608.01349](#)
39. P. Ko, Y. Omura, Y. Shigekami, C. Yu, LHCb anomaly and B physics in flavored Z' models with flavored Higgs doublets. *Phys. Rev. D* **95**(11), 115040 (2017). [arXiv:1702.08666](#)
40. R. Alonso, P. Cox, C. Han, T.T. Yanagida, Anomaly-free local horizontal symmetry and anomaly-free rare B-decays. *Phys. Rev. D* **96**(7), 071701 (2017). [arXiv:1704.08158](#)
41. Y. Tang, Y.-L. Wu, Flavor non-universal gauge interactions and anomalies in B-meson decays. *Chin. Phys. C* **42**(3), 033104 (2018). [arXiv:1705.05643](#). [Erratum: *Chin. Phys. C* **44**, 069101 (2020)]
42. D. Bhatia, S. Chakraborty, A. Dighe, Neutrino mixing and  $R_K$  anomaly in  $U(1)_X$  models: a bottom-up approach. *JHEP* **03**, 117 (2017). [arXiv:1701.05825](#)
43. K. Fuyuto, H.-L. Li, J.-H. Yu, Implications of hidden gauged  $U(1)$  model for B anomalies. *Phys. Rev. D* **97**(11), 115003 (2018). [arXiv:1712.06736](#)
44. L. Bian, H.M. Lee, C.B. Park, B-meson anomalies and Higgs physics in flavored  $U(1)'$  model. *Eur. Phys. J. C* **78**(4), 306 (2018). [arXiv:1711.08930](#)
45. R. Alonso, P. Cox, C. Han, T.T. Yanagida, Flavoured  $B - L$  local symmetry and anomalous rare B decays. *Phys. Lett. B* **774**, 643–648 (2017). [arXiv:1705.03858](#)
46. C. Bonilla, T. Modak, R. Srivastava, J.W.F. Valle,  $U(1)_{B_3-3L_\mu}$  gauge symmetry as a simple description of  $b \rightarrow s$  anomalies. *Phys. Rev. D* **98**(9), 095002 (2018). [arXiv:1705.00915](#)
47. S.F. King,  $R_{K^{(*)}}$  and the origin of Yukawa couplings. *JHEP* **09**, 069 (2018). [arXiv:1806.06780](#)
48. G.H. Duan, X. Fan, M. Frank, C. Han, J.M. Yang, A minimal  $U(1)'$  extension of MSSM in light of the B decay anomaly. *Phys. Lett. B* **789**, 54–58 (2019). [arXiv:1808.04116](#)
49. Z. Kang, Y. Shigekami,  $(g - 2)_\mu$  versus flavor changing neutral current induced by the light  $(B - L)_{\mu\tau}$  boson. *JHEP* **11**, 049 (2019). [arXiv:1905.11018](#)
50. L. Calibbi, A. Crivellin, F. Kirk, C.A. Manzari, L. Vernazza, Z' models with less-minimal flavour violation. *Phys. Rev. D* **101**(9), 095003 (2020). [arXiv:1910.00014](#)
51. W. Altmannshofer, J. Davighi, M. Nardecchia, Gauging the accidental symmetries of the standard model, and implications for the flavor anomalies. *Phys. Rev. D* **101**(1), 015004 (2020). [arXiv:1909.02021](#)
52. B. Capdevila, A. Crivellin, C.A. Manzari, M. Montull, Explaining  $b \rightarrow s\ell^+\ell^-$  and the Cabibbo angle anomaly with a vector triplet. *Phys. Rev. D* **103**(1), 015032 (2021). [arXiv:2005.13542](#)
53. J. Davighi, M. Kirk, M. Nardecchia, Anomalies and accidental symmetries: charging the scalar leptoquark under  $L_\mu - L_\tau$ . *JHEP* **12**, 111 (2020). [arXiv:2007.15016](#)
54. B.C. Allanach,  $U(1)_{B_3-L_2}$  explanation of the neutral current B-anomalies. *Eur. Phys. J. C* **81**(1), 56 (2021). [arXiv:2009.02197](#). [Erratum: *Eur. Phys. J. C* **81**, 321 (2021)]
55. D. Borah, L. Mukherjee, S. Nandi, Low scale  $U(1)_X$  gauge symmetry as an origin of dark matter, neutrino mass and flavour anomalies. *JHEP* **12**, 052 (2020). [arXiv:2007.13778](#)
56. A. Bednyakov, A. Mukhaeva, Flavour anomalies in a  $U(1)$  SUSY extension of the SM. *Symmetry* **13**(2), 191 (2021)
57. J. Davighi, Anomalous Z' bosons for anomalous B decays. [arXiv:2105.06918](#)
58. A. Greljo, Y. Soreq, P. Stangl, A.E. Thomsen, J. Zupan, Muonic force behind flavor anomalies. [arXiv:2107.07518](#)
59. X. Wang, Muon  $(g - 2)$  and flavor puzzles in the  $U(1)_X$ -gauged leptoquark model. [arXiv:2108.01279](#)
60. D. Bhatia, N. Desai, A. Dighe, Frugal  $U(1)_X$  models with non-minimal flavor violation for  $b \rightarrow s\ell\ell$  anomalies and neutrino mixing. [arXiv:2109.07093](#)
61. B.C. Allanach, J. Davighi, Naturalising the third family hypercharge model for neutral current B-anomalies. *Eur. Phys. J. C* **79**(11), 908 (2019). [arXiv:1905.10327](#)
62. B.C. Allanach, J.E. Camargo-Molina, J. Davighi, Global fits of third family hypercharge models to neutral current B-anomalies and electroweak precision observables. *Eur. Phys. J. C* **81**(8), 721 (2021). [arXiv:2103.12056](#)
63. J.M. Butterworth, D. Grellscheid, M. Krämer, B. Sarrazin, D. Yallup, Constraining new physics with collider measurements of Standard Model signatures. *JHEP* **03**, 078 (2017). [arXiv:1606.05296](#)

64. A. Buckley et al., Testing new physics models with global comparisons to collider measurements: the Contur toolkit. *SciPost Phys. Core* **4**, 013 (2021). [arXiv:2102.04377](#)
65. Particle Data Group Collaboration, P.A. Zyla et al., Review of particle physics. *PTEP* **2020**(8), 083C01 (2020)
66. C. Degrande, C. Duhr, B. Fuks, D. Grellscheid, O. Mattelaer, T. Reiter, UFO—the universal FeynRules output. *Comput. Phys. Commun.* **183**, 1201–1214 (2012). [arXiv:1108.2040](#)
67. A. Alloul, N. D. Christensen, C. Degrande, C. Duhr, B. Fuks, FeynRules 2.0—a complete toolbox for tree-level phenomenology. *Comput. Phys. Commun.* **185**, 2250–2300 (2014). [arXiv:1310.1921](#)
68. J. Bellm et al., Herwig 7.0/Herwig++ 3.0 release note. *Eur. Phys. J. C* **76**(4), 196 (2016). [arXiv:1512.01178](#)
69. M. Bahr et al., Herwig++ physics and manual. *Eur. Phys. J. C* **58**, 639–707 (2008). [arXiv:0803.0883](#)
70. C. Bierlich, A. Buckley, J.M. Butterworth, L. Corpe, D. Grellscheid, C. Gutsche, P. Karczmarczyk, J. Klein, L. Lonnblad, C.S. Pollard, H. Schulz, F. Siegert, Robust independent validation of experiment and theory: rivet version 3. *SciPost Phys.* **8**, 026 (2020). [arXiv:1912.05451](#)
71. E. Maguire, L. Heinrich, G. Watt, HEPData: a repository for high energy physics data. *J. Phys. Conf. Ser.* **898**(10), 102006 (2017). [arXiv:1704.05473](#)
72. S. Dulat, T.-J. Hou, J. Gao, M. Guzzi, J. Huston, P. Nadolsky, J. Pumplin, C. Schmidt, D. Stump, C.P. Yuan, New parton distribution functions from a global analysis of quantum chromodynamics. *Phys. Rev. D* **93**(3), 033006 (2016). [arXiv:1506.07443](#)
73. CMS Collaboration, A.M. Sirunyan et al., Measurement of the differential Drell-Yan cross section in proton-proton collisions at  $\sqrt{s} = 13$  TeV. *JHEP* **12**, 059 (2019). [arXiv:1812.10529](#)
74. ATLAS Collaboration, G. Aad et al., Measurement of the  $Z(\rightarrow \ell^+\ell^-)\gamma$  production cross-section in  $pp$  collisions at  $\sqrt{s} = 13$  TeV with the ATLAS detector. *JHEP* **03**, 054 (2020). [arXiv:1911.04813](#)
75. ATLAS Collaboration, G. Aad et al., Measurements of  $Z\gamma$  and  $Z\gamma\gamma$  production in  $pp$  collisions at  $\sqrt{s} = 8$  TeV with the ATLAS detector. *Phys. Rev. D* **93**(11), 112002 (2016) [arXiv:1604.05232](#)
76. ATLAS Collaboration, G. Aad et al., Measurements of  $W\gamma$  and  $Z\gamma$  production in  $pp$  collisions at  $\sqrt{s}=7$  TeV with the ATLAS detector at the LHC. *Phys. Rev. D* **87**(11), 112003 (2013). [arXiv:1302.1283](#). [Erratum: *Phys. Rev. D* **91**, 119901 (2015)]
77. ATLAS Collaboration, M. Aaboud et al., Measurements of the production cross section of a  $Z$  boson in association with jets in  $pp$  collisions at  $\sqrt{s} = 13$  TeV with the ATLAS detector. *Eur. Phys. J. C* **77**(6), 361 (2017)
78. CMS Collaboration, A. M. Sirunyan et al., Measurement of differential cross sections for  $Z$  boson production in association with jets in proton-proton collisions at  $\sqrt{s} = 13$  TeV. *Eur. Phys. J. C* **78**(11), 965 (2018). [arXiv:1804.05252](#)
79. LHCb Collaboration, R. Aaij et al., Measurement of forward  $W$  and  $Z$  boson production in association with jets in proton-proton collisions at  $\sqrt{s} = 8$  TeV. *JHEP* **05**, 131 (2016). [arXiv:1605.00951](#)
80. CMS Collaboration, A.M. Sirunyan et al., Measurement of associated production of a  $W$  boson and a charm quark in proton-proton collisions at  $\sqrt{s} = 13$  TeV. *Eur. Phys. J. C* **79**(3), 269 (2019). [arXiv:1811.10021](#)
81. ATLAS Collaboration, G. Aad et al., Measurements of top-quark pair differential and double-differential cross-sections in the  $\ell$ +jets channel with  $pp$  collisions at  $\sqrt{s} = 13$  TeV using the ATLAS detector. *Eur. Phys. J. C* **79**(12), 1028 (2019). [arXiv:1908.07305](#). [Erratum: *Eur. Phys. J. C* **80**, 1092 (2020)]
82. ATLAS Collaboration, G. Aad et al., Measurement of the low-mass Drell-Yan differential cross section at  $\sqrt{s} = 7$  TeV using the ATLAS detector. *JHEP* **06**, 112 (2014). [arXiv:1404.1212](#)
83. ATLAS Collaboration, G. Aad et al., Measurements of differential cross-sections in four-lepton events in 13 TeV proton-proton collisions with the ATLAS detector. *JHEP* **07**, 005 (2021). [arXiv:2103.01918](#)
84. Muon  $g - 2$  Collaboration, B. Abi et al., Measurement of the positive muon anomalous magnetic moment to 0.46 ppm. *Phys. Rev. Lett.* **126**, 141801 (2021). [arXiv:2104.03281](#)
85. F. Jegerlehner, A. Nyffeler, The Muon  $g-2$ . *Phys. Rep.* **477**, 1–110 (2009). [arXiv:0902.3360](#)
86. ATLAS Collaboration, Measurement of the  $\tau$  lepton reconstruction and identification performance in the ATLAS experiment using  $pp$  collisions at  $\sqrt{s} = 13$  TeV. *Tech. Rep. ATLAS-CONF-2017-029* (2017)
87. CMS Collaboration, A.M. Sirunyan et al., Performance of the CMS muon detector and muon reconstruction with proton-proton collisions at  $\sqrt{s} = 13$  TeV. *JINST* **13**(06), P06015 (2018). [arXiv:1804.04528](#)
88. ATLAS Collaboration, G. Aad et al., Muon reconstruction and identification efficiency in ATLAS using the full Run 2  $pp$  collision data set at  $\sqrt{s} = 13$  TeV. *Eur. Phys. J. C* **81**(7), 578 (2021). [arXiv:2012.00578](#)